Mineral crystal alignment in mineralized fracture callus determined by 3D small-angle X-ray scattering

To cite this article: Yifei Liu *et al* 2010 *J. Phys.: Conf. Ser.* **247** 012031

View the article online for updates and enhancements.

Related content

- A Microbeam Small-Angle X-ray Scattering Study on Enamel Crystallites in Subsurface Lesion
  N Yagi, N Ohta, T Matsuo et al.

- A SAXS/WAXS/GISAXS Beamline with Multilayer Monochromator
  Alexander Hexemer, Wim Bras, James Glossinger et al.

- Traceable size determination of PMMA nanoparticles based on Small Angle X-ray Scattering (SAXS)
  G Gleber, L Cibik, S Haas et al.

Recent citations

- Validation study of small-angle X-ray scattering tensor tomography
  Manuel Guizar-Sicairos *et al*

- Techniques to assess bone ultrastructure organization: orientation and arrangement of mineralized collagen fibrils
  Marios Georgiadis *et al*

- 3D scanning SAXS: A novel method for the assessment of bone ultrastructure orientation
  Marios Georgiadis *et al*

Mineral crystal alignment in mineralized fracture callus determined by 3D small-angle X-ray scattering

Yifei Liu[1], Inderchand Manjubala[1], Paul Roschger[2], Hanna Schell[3], Georg N Duda[3], and Peter Fratzl[1]

[1] Department of Biomaterials, Max Planck Institute of Colloids and Interfaces, 14424 Potsdam, Germany

[2] 4th Medical Department, Ludwig Boltzmann Institute of Osteology at Hanusch Hospital of WGKK and AUVA Trauma Centre Meidling, 1140 Vienna, Austria

[3] Julius Wolff Institut and Center for Musculoskeletal Surgery, Charité- University Medicine Berlin, Augustenburger Platz 1, 13353 Berlin, Germany

E-mail: fratzl@mpikg.mpg.de

Abstract. Callus tissue formed during bone fracture healing is a mixture of different tissue types as revealed by histological analysis. But the structural characteristics of mineral crystals within the healing callus are not well known. Since two-dimensional (2D) scanning small-angle X-ray scattering (sSAXS) patterns showed that the size and orientation of callus crystals vary both spatially and temporally [1] and 2D electron microscopic analysis implies an anisotropic property of the callus morphology, the mineral crystals within the callus are also expected to vary in size and orientation in 3D. Three-dimensional small-angle X-ray scattering (3D SAXS), which combines 2D SAXS patterns collected at different angles of sample tilting, has been previously applied to investigate bone minerals in horse radius [2] and oim/oim mouse femur/tibia [3]. We implement a similar 3D SAXS method but with a different way of data analysis to gather information on the mineral alignment in fracture callus. With the proposed accurate yet fast assessment of 3D SAXS information, it was shown that the plate shaped mineral particles in the healing callus were aligned in groups with their predominant orientations occurring as a fiber texture.

1. Introduction

As a functionally important tissue in all vertebrates, bone supports the body weight, enables functional movement and protects internal organs [4]. For these purposes, compact bone is known to have a fairly complicated hierarchical structure down to the nano level which contributes to its outstanding mechanical performances [5-8]. Although the structural features of bone are relatively well understood, the structural and mechanical properties of the fracture callus formed during bone fracture healing are not yet clear at a similar scale. It is observed by histology that during the formation, maturation and resorption of a callus, there are various types of tissue involved [9, 10]. Yet due to the spatially anisotropic and temporally dynamic property of callus composition, it is difficult to obtain accurate information of the callus characteristics in a three-dimensional manner [11-13].

From material composition point of view, mature bone mainly consists of two phases: organic phase (collagen) and inorganic phase (mineral). Both components as well as their interactions determine the mechanical behavior of bone [14]. One frequently used technique for the investigation of bone mineral crystals is small angle X-ray scattering (SAXS) [15, 16]. The advantage of this technique is that sample preparation is relatively easy and delicate local texture of the specimen can be acquired quantitatively. But the drawback is that only a cross section of the overall scattering pattern from the illuminated sample volume is able to be detected. This would lead to a considerable loss of information or could even result in misleading interpretation from the data, if the mineral crystals are expected to have a highly anisotropic behavior like in the fracture callus.

To overcome this drawback, three-dimensional (scanning and rotational) small angle X-ray scattering (3D SAXS), which was previously applied to investigate bone minerals in horse radius [2] and oim/oim mouse femur/tibia [3], is used here to reveal the spatial distribution of mineral crystal size and orientation in mineralized callus tissue of a sheep osteotomy model. Although the 3D-data accumulation is similarly realized through a controlled sample rotation as in those earlier studies, in the current work we propose a different routine of data analysis. The simple but effective representation of 3D SAXS data and the reconstruction of 3D SAXS patterns enable a direct visualization of mineral alignment in the investigated sample volume, which provides insight into the 3D structural properties of the callus material as well as their relation with its mechanical performance.

2. Materials and Methods

2.1. Sample Preparation

The sample investigated in this study comes from an earlier study [17] on fracture healing in a large animal model (female Merino sheep) of a 3 mm osteotomy stabilized with a monolateral external rigid fixator. Longitudinal section of bone/callus sample was harvested at 3 weeks time point of healing, fixed, dehydrated with ethanol, and embedded in polymethylmethacrylate (PMMA) without decalcifying. Using a low speed diamond saw (Buehler Isomet, Buehler GmbH, Duesseldorf, Germany), a 200 µm section was cut from the embedded block for 3D SAXS evaluation. Experimental regions of interest (ROIs) were chosen within the periosteal callus on the medial side of the proximal fragment (figure 1). The positions of ROIs were defined to have comparison with the previously reported structural properties of the callus [1].
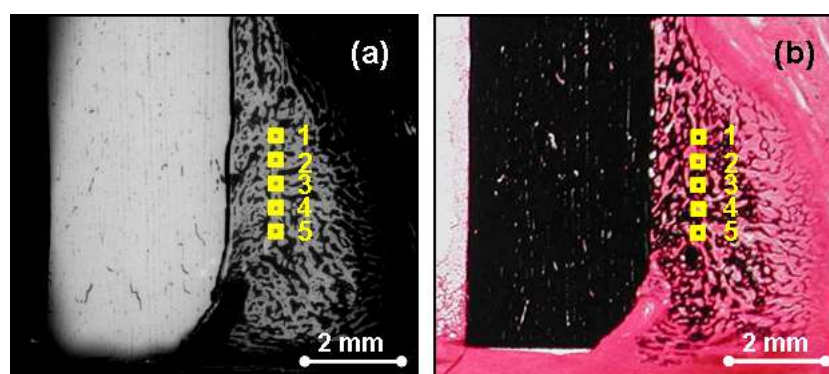

Figure 1. Regions of interest were chosen in the periosteal callus formed at 3 weeks of healing, on the medial side of the proximal fragment. Altogether five positions (ROI 1 to 5, marked in yellow) with a same transversal distance from the adjacent cortex were experimentally evaluated by 3D SAXS. Backscattered electron image (figure a) and Safranin Orange/von Kossa staining (figure b) show an abundant but anisotropic bone formation within the callus.

2.2. SAXS Measurements

3D small-angle X-ray scattering was done with a laboratory SAXS instrument (Nanostar, Bruker AXS, Karlsruhe, Germany). X-ray beam (*Cu-Kα*, *λ* = 0.1542 nm) is generated with a rotating Cu anode generator (M06XCE– SRA, Mac Science, Japan) operated at 4 kW (40 kV, 100 mA) and is collimated by a double pinhole system (first pinhole diameter 100 μm, second pinhole diameter 300 μm). Sample is mounted on a translation stage with three degrees of freedom (translation axes *x* and *y* within the sample plane and rotation axis *z* perpendicular to the beam). 2D scanning (scanning small-angle X-ray scattering, sSAXS) over the sample is realized via automatic movement of the sample stage in *x* and *y* directions with a resolution of 200 μm (real space resolution) which is equivalent to the thickness of sample slice as well as the beam diameter at the sample position (focal plane). 3D SAXS is done by additionally applying a sample rotation along *z* axis. The scattering pattern is collected with an accumulation time of 3600 seconds on a two-dimensional CCD detector of 1024×1024 pixels with pixel size of 105.26 μm (reciprocal space resolution) placed at a distance of 600 mm behind the specimen. All the chambers are evacuated to avoid air scattering. A schematic overview of the whole experimental setup is shown in figure 2.
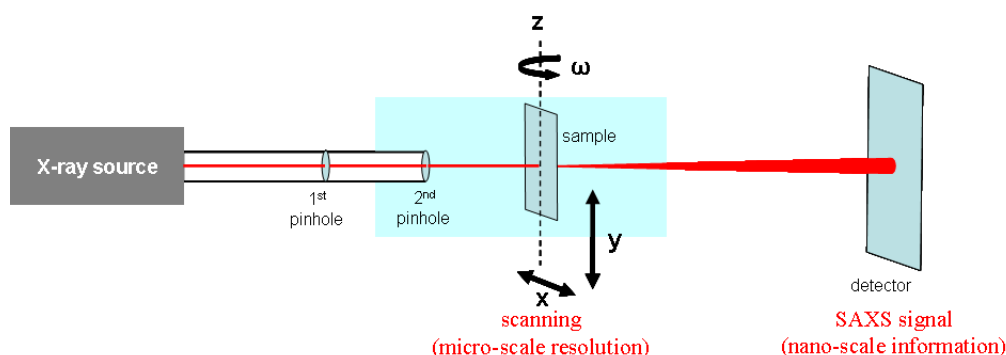

Figure 2. Schematic view of the experimental set-up, which is typically the same for 3D SAXS. Similar to 2D sSAXS, movement of the sample is possible in *x* and *y* directions. But additionally, the sample is rotated around the vertical axis *z* by an angle *ω* to gain texture information in the third dimension.

In this study, the sample was rotated around the vertical axis *z* in steps of 15° from -45° to 45°, leading to seven rotation angles. For each rotation angle *ω* (-45° ≤ *ω* ≤ 45°), a 2D X-ray radiograph (absorption image) of the whole sample was generated by using a pin-diode. Regions of interest chosen to be located along a vertical line were marked by two parallel sharp knife edges attached onto the sample, and the corresponding x-y motor positions were defined for SAXS measurements according to the seven radiographs. 2D SAXS patterns were by this means always collected at the same five positions on the specimen as illustrated in figure 1 for all the rotation angles, which enables the reconstruction of the five 3D SAXS patterns in reciprocal space.

The calibration of the beam center and scattering distance was done at each angle *ω* by measuring a silver behenate (AgBh) standard sample. 2D SAXS patterns were all corrected for transmission rate derived from radiography, background scattering (empty beam) and detector noise reduction (dark current).

2.3. Data Analysis

2.3.1. *1D normalization.*
Particularly due to the change of effective sample thickness (along the beam direction) during sample rotation, a normalization factor (NF) has to be calculated from the series of 2D SAXS patterns acquired at the same sample position to correct the change in SAXS intensity caused by the change in illuminated sample volume. This was realized by integrating a total SAXS

intensity of the 2D SAXS pattern along a vertical line across the beam center (*v* axis in figure 3b, or *z* axis in figure 3d, both in reciprocal space). Practically a radial integration was applied to the circulator sectors of -0.5° < χ < 0.5° and -179.5° < χ < 180.5° within a fixed radial range (50 pixels < *r* < 420 pixels, 0.34 nm^{-1} < *q* < 2.83 nm^{-1}, 0.5° < 2θ < 4.2°) at all seven ω angle positions. χ is the azimuthal angle as defined in figure 3d. *q* is the modulus of the scattering vector defined as $q = \dfrac{4\pi}{\lambda}\sin\theta$, where 2$\theta$ is the scattering angle and λ is the X-ray wavelength. Inner radius r_1 was set to be 50 pixels for avoiding scattering influence from the beam stop, and outer radius r_2 was set to be 420 pixels for keeping the integrated region inside the detector range. The integrated intensities within circulator sectors of -0.5° < χ < 0.5° and -179.5° < χ < 180.5° were then averaged to obtain a constant K(ω) depending only on the rotation angle of the specimen. The ratio NF(ω) = K(ω) / K(0) was taken as a normalization factor for each scattering pattern obtained at any given rotation angle ω. Table 1 gives a summary of the normalization factors for all the five regions of interest at all the seven rotation angles.
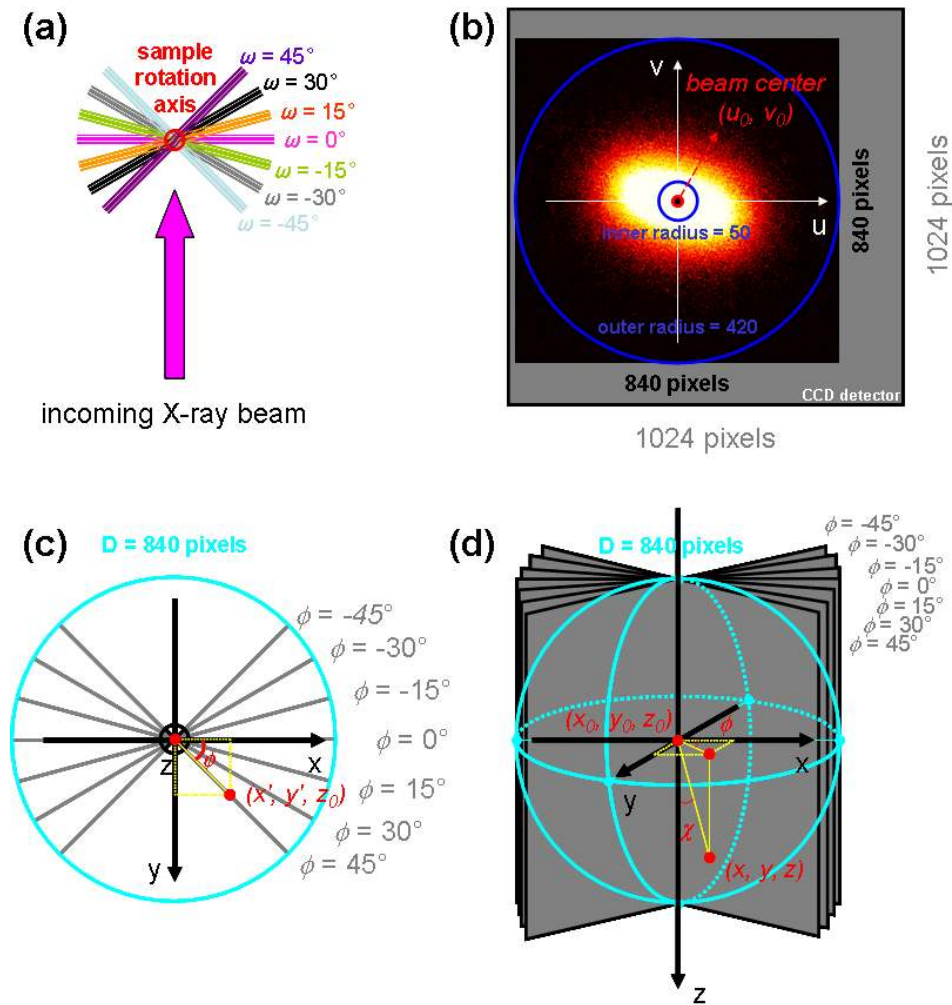

Figure 3. Sample rotation in real space (figure a) is characterized by the rotation angle ω. Measured SAXS pattern (figure b) representing reciprocal space is characterized by the angular position ϕ (figure c) of the detector with respect to the sample, and additionally by the azimuthal angle χ which lies in the detector plane (figure d).

Table 1. Normalization factors NF(ω) of the five regions of interest on the sample at different rotation angles (-45° $\leq \omega \leq$ 45° with a step of 15°).

	NF (ROI 1)	NF (ROI 2)	NF (ROI 3)	NF (ROI 4)	NF (ROI 5)
ω = 45°	1.4375	1.3716	2.0033	1.2581	1.2163
ω = 30°	1.0244	1.6131	1.3503	1.1230	0.9953
ω = 15°	1.0504	1.1827	1.3110	1.1637	0.9722
ω = 0°	1.0000	1.0000	1.0000	1.0000	1.0000
ω = -15°	0.9307	1.2313	1.3722	0.7827	0.8379
ω = -30°	0.7882	1.7248	1.2627	1.7890	0.7852
ω = -45°	1.0236	1.8978	1.6243	1.9608	0.9563

Using this normalization procedure ensures that the SAXS intensity does not change with rotation in the direction of the rotation axis. In this way, we correct for the changes in effective sample volume when the section is rotated. The limitation of this procedure is, however, that the projection of the X-ray beam on the specimen also changes with rotation. Hence, the procedure is only exact if the nanostructure (as studied by SAXS) stays approximately the same within the different probing volumes when the rotation angle ω varies. Figure 4 describes the intensity profiles (azimuthally integrated) of the first ROI before and after normalization.
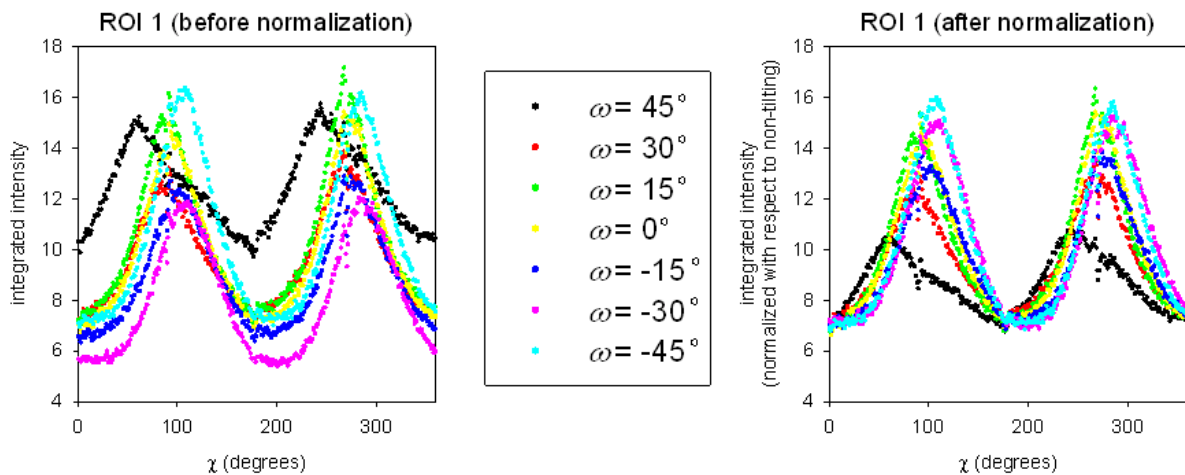

Figure 4. Intensity profiles (azimuthally integrated) of the first region of interest before (left) and after (right) normalization using the factors in Table 1. The measured intensity was initially the highest at ω = ±45° because rotation induced an increase of the illuminated sample volume. This is corrected by the normalization.

2.3.2. *2D representation.* For small-angle X-ray scattering the Ewald sphere can be considered to be flat. Therefore scattering patterns at different rotation angle ω correspond to cross sections of the 3D SAXS "ellipsoids" in reciprocal space at different angular position ϕ. Considering that ω is the angle between the sample plane and the detector plane (figure 3), we have $\phi = -\omega$.

For each of the five ROIs at the sample, 1D $I(\chi)$ profiles were deduced for different ω positions (ϕ positions) by azimuthal integration of all the 2D SAXS patterns within the fixed radial range from r_1 to r_2 around the direction of the incoming X-ray beam. $I(\chi, \phi)$ was then plotted in a 2D manner to illustrate the orientation of the scattering pattern in 3D. Normalization factors (Table 1) were used to scale the whole $I(\chi)$ spectrum for normalizing $I(\chi, \omega)$ at χ = 0° and χ = 180°. $I(\chi)$ values at unavailable ω positions (ϕ positions) were linearly interpolated.

2.3.3. *3D visualization.* Assume that n 2D measurements $g_1(u,v)$, $g_2(u,v)$,…, $g_n(u,v)$ with detector coordinates u and v (figure 3b) were acquired at angular positions ϕ_1, ϕ_2,…, ϕ_n respectively, and the angular positions satisfy $-45° \leq \phi_1 < \phi_2 < \ldots < \phi_n \leq 45°$ (figure 3c and 3d). Then the value of each voxel in the reconstructed volume, $f(x,y,z)$, can be calculated as (figure 3c and 3d):

$$f(x,y,z) = \begin{cases} \dfrac{(\phi_{i+1} - \hat{\phi})g_i(l,z') + (\hat{\phi} - \phi_i)g_{i+1}(l,z')}{\phi_{i+1} - \phi_i} & \phi_i \leq \hat{\phi} < \phi_{i+1} \\[4mm] \dfrac{(\phi_{i+1} + 180° - \hat{\phi})g_i(l,z') + (\hat{\phi} - \phi_i - 180°)g_{i+1}(l,z')}{\phi_{i+1} - \phi_i} & \phi_i + 180° \leq \hat{\phi} < \phi_{i+1} + 180° \quad (1), \\[4mm] 0 & \text{else} \end{cases}$$

$$\text{where } \hat{\phi} = \begin{cases} \arctan \dfrac{x - x_0}{y - y_0} & x - x_0 \geq 0, y \neq y_0 \\[3mm] \arctan \dfrac{x - x_0}{y - y_0} + 180° & x - x_0 < 0, y \neq y_0, \\[3mm] 0 & y = y_0 \end{cases}$$

$$l = \sqrt{(x - x_0)^2 + (y - y_0)^2},$$

and $z' = z - z_0 + u_0$.

In these equations, x_0, y_0 and z_0 define the center position (origin) of the reconstructed volume and i is the number of 2D measurement which satisfies $1 \leq i \leq n\text{-}1$. The 3D spherical volume with the dimension of $d = 840$ pixels was reconstructed by equation (1) from the series of 2D measurements done at different sample rotation angle ω. Normalization factors for normalizing $I(\chi, \omega)$ in the previous section were also used here to scale the intensity of the raw SAXS patterns before coordinate conversion.

To interpret the directionality of the reconstructed 3D volume with 2D plots, integral values for all the ray directions with different azimuth angles ϕ ($\phi_1 \leq \phi \leq \phi_n$) and inclination angles χ ($0° \leq \chi < 360°$) from the origin of the volume were calculated (figure 3d), with 1° interval for both ϕ and χ. In order to avoid the anisotropic shadow from the beam stop and to balance the integral length for all the directions, the rays within the lengths of inner radius r_1 (50 pixels) and outer radius r_2 (420 pixels) from the origin (beam center) were integrated. r_1 and r_2 were chosen such to match the effective q range (0.34 nm^{-1} < q < 2.83 nm^{-1}) defined before. The integrations along such ray paths were calculated with Siddon ray tracing algorithm [18].

3. Results and Discussion
Figure 5 illustrates the 2D orientation figure $I(\chi, \phi)$ of all the five investigated sample volumes (200 μm × 200 μm × 200 μm each) at the five ROIs.

In all the five ROIs, apart from the existence of two periodic maximums appearing along the χ axis with a spacing of 180° due to the complete symmetry of the 3D SAXS ellipsoid, it turns out that there are also more than one global maximum along the ϕ axis. The intensity maps always show two separate groups of intensity concentration in this direction, indicating an overlaying of two ellipsoids in 3D reciprocal space. This agrees with results from previous sSAXS measurements which reveal in some cases a 2D SAXS pattern of spark instead of oval [1].

The dash lines (marked in black) in $I(\chi, \phi)$ figures correspond to stacks of mineral crystals with different amount (relative value of normalized intensity) and orientation (peak position of normalized intensity) within the illuminated sample volume. It can be seen that each dash line is made up of a series of neighboring maximums (with respect to the other intensities at the same ϕ position) reflecting a gradual change of the preferred mineral orientation. Knowing that the directionality of SAXS pattern

in reciprocal space is perpendicular to the orientation of mineral crystals in real space, it can be further concluded that the 3D SAXS pattern has a tendency of being an oblate spheroid.
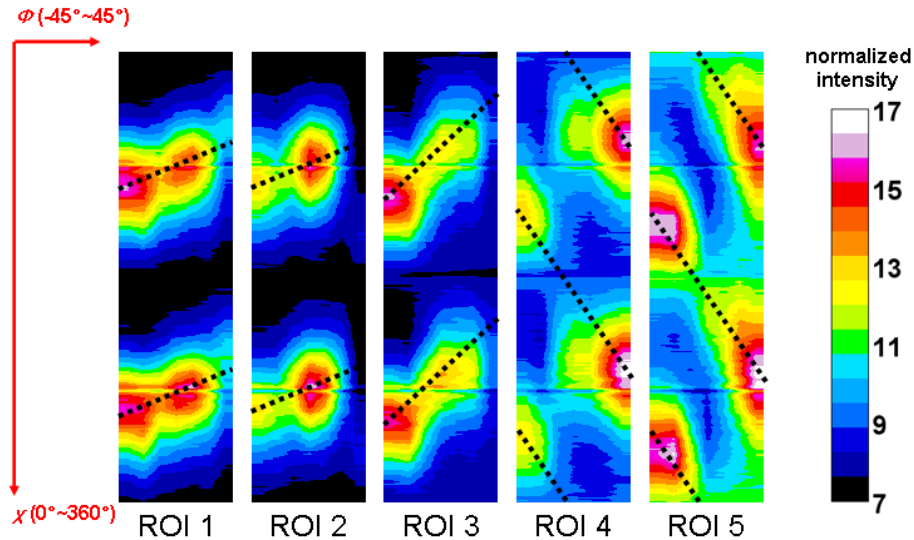

Figure 5. 2D orientation figure $I(\chi, \phi)$ of the five ROIs. Normalized intensities are shown with colour-coding.

Figure 6 demonstrates the integral values for different ϕ and χ angles of one ROI with 2D orientation figure $I(\chi, \phi)$, calculated from the reconstructed 3D volume using the Siddon ray tracing algorithm. Compared to the $I(\chi, \phi)$ plot got from direct linear interpolation (figure 5, ROI 1), the obtained $I(\chi, \phi)$ orientation figure here (figure 6) has higher intensity caused by finer integration scheme. And in the latter figure, the calculation procedure from 1D to 3D and back to 2D has led to some artifacts at $\phi = 0°$, $\chi = 0°$, and $\chi = \pm180°$. Nevertheless the two results are basically in good agreement with each other. The global maximum of the directionality occurs at the position of $\phi = -30.0° \pm 7.5°$ and $\chi = 285° \pm 2°$. This means, if without the need of 3D visualization, a direct plotting of the 2D orientation figure $I(\chi, \phi)$ should be precise enough and maybe even better (free from artifacts) to depict the mineral alignment in 3D.
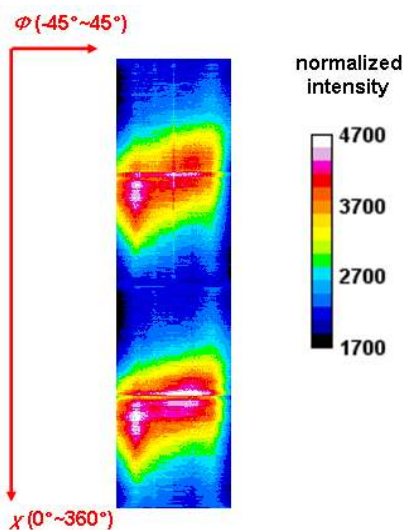

Figure 6. 2D orientation figure $I(\chi, \phi)$ of the first ROI, calculated from the reconstructed 3D volume with Siddon ray tracing algorithm. Normalized intensities are shown with colour-coding.

Based on one of the proposed models of mineralized fibrils [19], SAXS-pattern direction (orientation in reciprocal space, red arrows in figure 7) of the mineral crystal stacks should form a normal plane of the fiber direction (orientation in real space, perpendicular to the plane of figure 7). The general idea is that the X-ray beam (due to the size of its cross-sections) covers many mineralized collagen fibrils (with a typical diameter in the order of 100 nm) where the mineral crystals (plates viewed edge-on in figure 7) are oriented differently in different groups of fibrils. This leads to a SAXS pattern in the shape of an oblate ellipsoid. The direction of the ellipsoid axis can be read from the patterns in figure 5 and corresponds to the perpendicular to the broken line. Since the ellipsoid is not perfect in the sense that the intensity varies around the rotation axis (that is, along the broken line in figure 5), we conclude that there is a certain texture in the orientation distribution of the crystals. Maps such as the ones described in figure 5 can be used to quantify their orientation distribution.
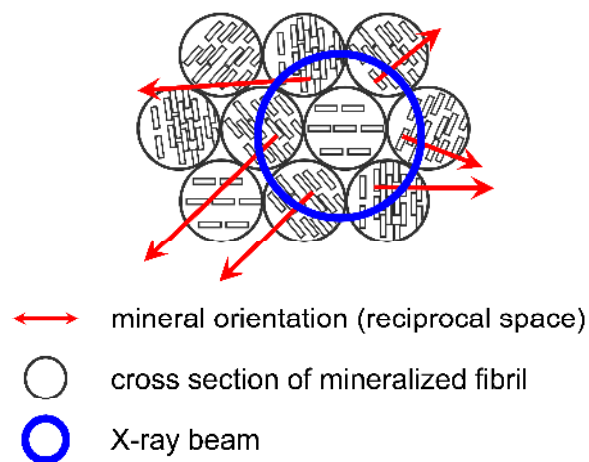

mineral orientation (reciprocal space)

cross section of mineralized fibril

X-ray beam

Figure 7. Illustration of circular dispersion of crystals in normal bone illuminated by a 200 μm beam (not drawn to scale), adapted from a previously proposed model of mineralized fibrils [19]. Fiber orientation in real space (not depicted) is perpendicular to the plane of the paper, and the red arrows show mineral orientations in reciprocal space for mineral crystals within the beam area indicated by solid blue ring.

4. Conclusion

In this study, a simple and effective method to visualize and interpret the 3D directionality of SAXS results obtained from sheep fracture callus is presented. Interpretation of the 3D directionality via 2D plotting gives accurate information of the mineral orientation within bony structure at specific positions of the sample. 3D reconstruction of the full SAXS patterns in reciprocal space enables quantitative determination and visualization of the global directionality of the overall SAXS pattern. As a main result of the current study concerning the structural properties of callus minerals, it was shown that the mineral particles were aligned in stacks with their predominant orientations lying in a single plane perpendicular to the fiber direction.

References

[1]   Liu Y, Manjubala I, Roschger P, Epari D R, Schell H, Lienau J, Bail H J, Duda G N and Fratzl P 2009 The evolution of size and distribution of apatite mineral crystals during bone fracture healing in sheep *Bone* **44** S271-S2

[2]   Fratzl P, Schreiber S and Boyde A 1996 Characterization of bone mineral crystals in horse radius by small-angle X-ray scattering *Calcif. Tissue Int.* **58** 341-6

[3]   Fratzl P, Paris O, Klaushofer K and Landis W J 1996 Bone mineralization in an osteogenesis imperfecta mouse model studied by small-angle X-ray scattering *J. Clin. Invest.* **97** 396-402

[4]   Carter D R and Beaupre G S 2001 *Skeletal function and form: mechanobiology of skeletal development, aging, and regeneration* (New York: Cambridge University Press)

[5]   Lakes R 1993 Materials with structural hierarchy *Nature* **361** 511-5

[6]   Rho J Y, Kuhn-Spearing L and Zioupos P 1998 Mechanical properties and the hierarchical structure of bone *Med. Eng. Phys.* **20** 92-102

[7]   Weiner S and Wagner H D 1998 The material bone: structure-mechanical function relations *Annu. Rev. Mater. Sci.* **28** 271-98

[8]   Fratzl P and Weinkamer R 2007 Nature's hierarchical materials *Prog. Mater. Sci.* **52** 1263-334

[9]   Hall B 2005 *Bones and cartilage: developmental and evolutionary skeletal biology* (London: Elsevier Academic Press)

[10] Shapiro F 2008 Bone development and its relation to fracture repair. The role of mesenchymal osteoblasts and surface osteoblasts *Eur. Cells Mater.* **15** 53-76

[11] Hildebrand T, Laib A, Muller R, Dequeker J and Ruegsegger P 1999 Direct three-dimensional morphometric analysis of human cancellous bone: microstructural data from spine, femur, iliac crest, and calcaneus *J. Bone Miner. Res.* **14** 1167-74

[12] Cann C E 1988 Quantitative CT for determination of bone mineral density: a review *Radiology* **166** 509-22

[13] Gerstenfeld L C, Alkhiary Y M, Krall E A, Nicholls F H, Stapleton S N, Fitch J L, Bauer M, Kayal R, Graves D T, Jepsen K J and Einhorn T A 2006 Three-dimensional reconstruction of fracture callus morphogenesis *J. Histochem. Cytochem.* **54** 1215-28

[14] Fratzl P, Gupta H S, Paschalis E P and Roschger P 2004 Structure and mechanical quality of the collagen-mineral nano-composite in bone *J. Mater. Chem.* **14** 2115-23

[15] Fratzl P, Fratzlzelman N, Klaushofer K, Vogl G and Koller K 1991 Nucleation and growth of mineral crystals in bone studied by small-angle X-ray scattering *Calcif. Tissue Int.* **48** 407-13

[16] Fratzl P, Groschner M, Vogl G, Plenk H, Eschberger J, Fratzlzelman N, Koller K and Klaushofer K 1992 Mineral crystals in calcified tissues: a comparative study by SAXS *J. Bone Miner. Res.* **7** 329-34

[17] Schell H, Lienau J, Epari D R, Seebeck P, Exner C, Muchow S, Bragulla H, Haas N P and Duda G N 2006 Osteoclastic activity begins early and increases over the course of bone healing *Bone* **38** 547-54

[18] Siddon R L 1985 Fast calculation of the exact radiological path for a three-dimensional CT array *Med. Phys.* **12** 252-5

[19] Rubin M A, Jasiuk I, Taylor J, Rubin J, Ganey T and Apkarian R P 2003 TEM analysis of the nanostructure of normal and osteoporotic human trabecular bone *Bone* **33** 270-82